Computational cell quantification in the human brain tissues based on hard X-ray phase-contrast tomograms

Simone E. Hieber[a], Christos Bikis[a], Anna Khimchenko[a], Georg Schulz[a], Hans Deyhle[a], Peter Thalmann[a], Natalia Chicherova[a,b], Alexander Rack[c], Marie-Christine Zdora[d], Irene Zanette[d], Gabriel Schweighauser[e], Jürgen Hench[e], and Bert Müller[a]

[a]Biomaterials Science Center, Department of Biomedical Engineering, University of Basel, Gewerbestrasse 14, 4123 Allschwil, Switzerland
[b]Medical Image Analysis Center, Department of Biomedical Engineering, University of Basel, Gewerbestrasse 14, 4123 Allschwil, Switzerland
[c]European Synchrotron Radiation Facilities (ESRF), 71 avenue des Martyrs, 38000 Grenoble, France
[d]Diamond Light Source, Harwell Science and Innovation Campus, Didcot, Oxfordshire OX11 0DE, UK
[e]Institute of Pathology, Department of Neuropathology, University Hospital of Basel, 4001 Basel, Switzerland

ABSTRACT

Cell visualization and counting plays a crucial role in biological and medical research including the study of neurodegenerative diseases. The neuronal cell loss is typically determined to measure the extent of the disease. Its characterization is challenging because the cell density and size already differs by more than three orders of magnitude in a healthy cerebellum. Cell visualization is commonly performed by histology and fluorescence microscopy. These techniques are limited to resolve complex microstructures in the third dimension. Phase-contrast tomography has been proven to provide sufficient contrast in the three-dimensional imaging of soft tissue down to the cell level and, therefore, offers the basis for the three-dimensional segmentation. Within this context, a human cerebellum sample was embedded in paraffin and measured in local phase-contrast mode at the beamline ID19 (ESRF, Grenoble, France) and the Diamond-Manchester Imaging Branchline I13-2 (Diamond Light Source, Didcot, UK). After the application of Frangi-based filtering the data showed sufficient contrast to automatically identify the Purkinje cells and to quantify their density to 177 cells per mm^3 within the volume of interest. Moreover, brain layers were segmented in a region of interest based on edge detection. Subsequently performed histological analysis validated the presence of the cells, which required a mapping from the two-dimensional histological slices to the three-dimensional tomogram. The methodology can also be applied to further tissue types and shows potential for the computational tissue analysis in health and disease.

Keywords: single-distance propagation-based tomography, X-ray tomography, phase contrast, cell segmentation, synchrotron radiation, neuronal cells, human cerebellum.

1. INTRODUCTION

The human cerebellum as a particular example of brain tissue shows the characteristic distribution of white and gray matter, as well as the three-layer structure of the cerebellar cortex. In the middle layer there exist the distinctively large Purkinje cells, which have been favored for histological observations. The cerebellum is a structure of prime interest based on its function too. From early on, it has been identified as an integral component of motor function and control, regulating coordination and balance, fine motion, posture and gait.[1] In clinical practice, cerebellar dysfunction can usually be quickly revealed by a standard neurological examination,

---

Further author information: (Send correspondence to Simone Hieber):
E-mail: Simone Hieber: E-mail: simone.hieber@unibas.ch , Telephone: +41 61 207 54 41

making the connection between microscopic observations in the basic research field and patient symptoms or signs exceedingly direct. During the last twenty to thirty years, the introduction and widespread use of functional imaging methods, supported by the considerable evolution of structural imaging in terms of resolution, versatility and reliability, have led to a reevaluation of the cerebellum's role as being exclusively a motor control center. Today's state of research recognizes the cerebellum's involvement, among others, in memory, learning, emotion, behavior and language.[2]

In vivo methods including magnetic resonance imaging (MRI) are important particularly in clinical practice, but cannot reach the cellular resolution. Thus, *ex vivo* techniques are required to reach true cellular, as well as sub-cellular resolution. Brightfield microscopy of histological slices, optical coherence scanning, confocal microscopy and light sheet illumination, have been used to visualize tissue slices of up to 200 micrometers in thickness, or even whole mouse brains, with or without the need for serial sectioning. This way the cerebellar structure has been studied together with the changes that take place during its development.[3–5] Recently, the CLARITY protocol has been introduced to clear murine brain tissue for flourescence microscopy.[6] Although being an interesting approach, its shortcomings lie in the advanced technical protocol, the limitation to one antibody used at a time, and the loss of the specimen for further investigations. Within this context, X-ray phase-contrast tomography provides a promising solution for the three-dimensional brain tissue visualization prior to histological sectioning.[7,8] Very recently, our research group reported the significant improvement of brain tissue contrast for tomography by standard paraffin embedding of the specimens. The performance was demonstrated for absorption contrast in a conventional laboratory device[9] and for phase-contrast tomography using synchrotron radiation.[10]

In this study we compare the results of phase-contrast tomography with brightfield microscopy of standard histological slices. Moreover we illustrate the quantification of cells and segment two main brain layers in two and three dimensions.

2. MATERIALS AND METHODS

2.1 Specimen preparation and histology

Human cerebellum specimens were extracted *post mortem* from a brain of a 73 year-old male. The specimens were fixed in 4% histological grade buffered formalin, dehydrated in ethanol, transferred to xylenes and embedded in a paraffin/plastic polymer mixture (Surgipath Paraplast, Leica Biosystems, Switzerland). Cylindrical-shaped paraffin blocks with a diameter of 6 and 3 mm were extracted as illustrated in Figure 1. After the scans the larger specimen was sliced into 4 μm-thick slides for histological staining to validate the findings. More details can be found in the references.[9,10]
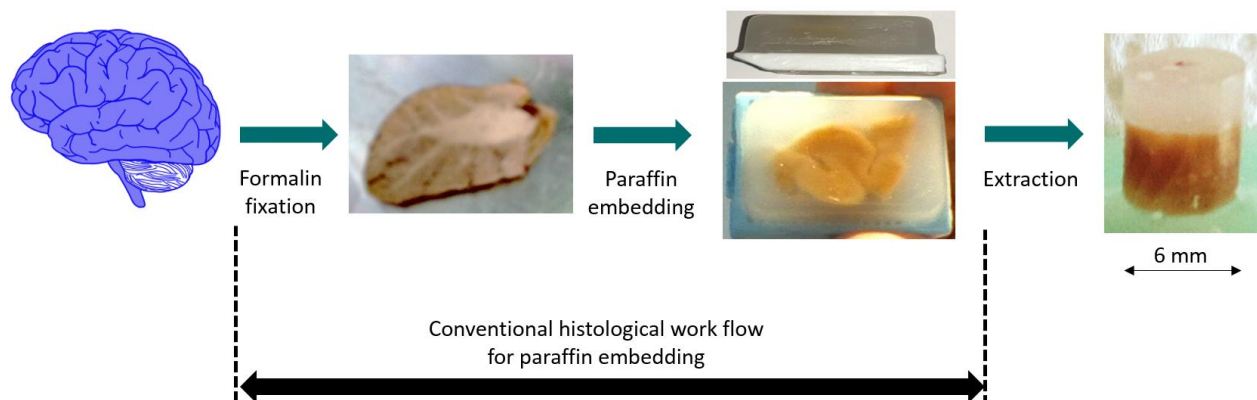

Figure 1. The specimen preparation includes the standard protocol for paraffin-embedding which is also used for the histological analysis of autopsies and biopsies. Furthermore, a cylinder was prepared for three-dimensional imaging using phase-contrast tomography at synchrotron radiation facilities.

2.2 Data acquisition

Since the sample diameter was bigger than the detector field-of-view (FOV), measurements were performed in local tomography configurations. The single-distance X-ray tomography was performed at two synchrotron facilities. The specimen with a diameter of 6 mm was scanned at the beamline ID 19 (ESRF, Grenoble, France)[11] with an effective pixel size of 1.75 µm and a mean photon energy of 19.45 keV. The detection system was a FReLoN 2K CCD with 2048×2048 pixels. The two height steps covered a cylindrical volume with a diameter of 3.5 mm and a height of 4.5 mm. Projections were acquired at a propagation distance of 80 cm. Images were taken at 2004 equi-angular steps over 360 degrees with an exposure time of 1 s per raw image.

The specimen with a volume of 3 mm^3 was scanned at Diamond-Manchester Imaging Branchline I13-2 (Diamond Light Source, Didcot, UK).[12] The effective pixel size was 0.45 µm and a photon energy 19 keV. The pco.4000 scintillator-based X-ray detector (PCO AG, Kelheim, Germany) had 4008×2672 pixels. The reconstructed volume had a diameter of 1.6 mm and a height of 1.6 mm. Images were taken at a distance of 5 cm and with an exposure time of 8 s per raw image for 2400 equi-angular steps over 180 degrees.

The phase-shift profiles of the specimens were determined by a standard single-distance phase retrieval procedure. Phase-contrast was recovered from a single projection taken at a defined specimen-detector distance, generated by the free-space propagation of X-rays.[13, 14] Measurement sample-detector distances were selected based on the contour plot of the critical propagation distances for various pixel sizes and photon energies.[15]

Flat-field and dark-field corrections of local tomography data were performed using the software ANKAphase[15] with the input parameter $\delta/\beta = 2406$, where δ/β is the ratio of the refractive index decrement over the absorption coefficient of paraffin at the given energy and distance. Phase recovery was performed based on a single-distance, non-iterative, phase-retrieval algorithm with flat-field correlation and the ratio δ/β as input parameter.

The tomographic reconstruction of the data used the filtered back-projection (FBP) method with a standard Ram-Lak filter. Both steps were employed by in-house implementations in Matlab$^{\circledR}$ R2014b (Simulink, The MathWorks, Inc., USA).

Radial gradients and ring artefacts were reduced prior to tomographic reconstruction, using zero-padding and a combined wavelet-Fourier filtering technique,[16] and then applied to the sinograms in the reconstruction procedure.

2.3 Data quantification

2.3.1 2D-3D registration

To register a histological slice within the three-di-mensional phase tomogram, we applied an automatic 2D-3D registration algorithm, an extension of the previous work of Chicherova et al.[17, 18] A first match was identified according to the published algorithm in a dataset covering the entire diameter of the specimen. We applied the scale- and rotation-invariant feature detector and descriptor SURF[19] to both the tomogram and the histological slice, to find matching feature points in the 3D dataset. Plane fitting to the filtered point cloud led to an estimation of the slice position and orientation. After registering the found virtual CT slice with its histological counterpart in 2D, positioning was refined by reapplying the described approach with self-similarity[20] as a feature point detector. Finally, the resulting set of plane parameters was transferred, in order to extract the matching slice from the local tomography dataset.

2.3.2 Purkinje cell segmentation

Due to local intensity gradients, the inline tomograms overlap and a thresholding approach cannot be used for segmentation. As a result, we developed a segmentation algorithm based on Frangi filter that can identify cells according to their geometry. The Frangi filter determines the probability of a voxel to belong to a tubular structure (Aharinejad et al., 1998; Frangi et al., 1998). For that purposes, it computes the eigenvalues $\lambda = (\lambda_1, \lambda_2, \lambda_3)$ of the 3D Hessian matrix. To segment the Purkinje cells only, the scale range was chosen 3 to 6 voxels (5.25 to 10.5 µm), the sensitivity parameters $\alpha = 0.2, \beta = 0.5$ and $\gamma = 40$ and objects smaller than 300 voxels (1600 µm^3) were neglected. All parameter and thresholds were chosen by visual inspection to avoid the segmentation of noisy structures. A level set representation was used to visualize the segmented objects and to categorize their geometry. The *Corpora amylacea*, accumulations of calcium without functionality, could be

identified by an absolute mean level set value larger than 12 due to their spherical shape. The ratio between the object size and the mean level set value squared was above 450 for tubular structures indicating thick vessels in this case. Both object types were detected by the Frangi filter and could be sorted by the criteria above. The filter was sufficiently stable with respect to the involved local gradients in the data set. More details can be found in a very recent publication of our research group.[10]

2.3.3 Brain layer segmentation

The standard thresholding segmentation of the brain layers was hindered by the local gradients in the data set. Preprocessing steps were necessary to eliminate the effect of gradients. First, an edge detection was performed by subtracting a smoothed data set from the original one. This approach can be refered to a gaussian-based edge-detection method.[21] The profile of edge density provided sufficient contrast to distinguish the brain layers after 4-fold binning. The increase of image quality was already reported by Thurner *et al.*[22] The layers were finally segmented by thresholding according to Otsu.[23] The brain layers considered were the *Stratum granulosum* and *Stratum moleculare*. By applying the threshold to two-dimensional slices, the *Stratum granulosum* could be detected whereas Otsu threshold in 3D identified the *Stratum granulosum* and the Purkinje cell layer together. By combining the segmentation results in a region of interest, the *Stratum moleculare* was identified.

The algorithm consists of the following main steps

1. Edge detection to remove gradient

2. 4-fold binning to increase density resolution of edge information

3. Otsu thresholding

4. Filling holes within the segmented region

5. Extrapolation to original data size and smoothing

3. RESULTS AND DISCUSSION

The following section presents the results of the tomographic scans, their comparison to histological findings and the cell/brain layer identification. The grayscale of tomographic images is inverted to achieve a better visual matching with the staining intensity of the histological slides.

3.1 Comparison of tomogram and histological slide

In general, histology can suffer from slicing or staining artifacts and is not favorable for three-dimensional structure analysis because of the demanding preparation time and the anisotropic resolution in comparison to computed tomography. Figure 2 shows a circular area of the tomogram (A) which was registered to histological slide (B) automatically. The tomogram features light gradients, but the microstructure of the human brain is well recognizable. The brain layers and vessels are clearly visible. Since the specimen was required to be re-embedded after the scan, the correspondence is not homogenous in the considered area. The matching is better for the brain layers than for the vessels. A registration with a curved surface would be required to achieve a better matching as performed recently.[9]
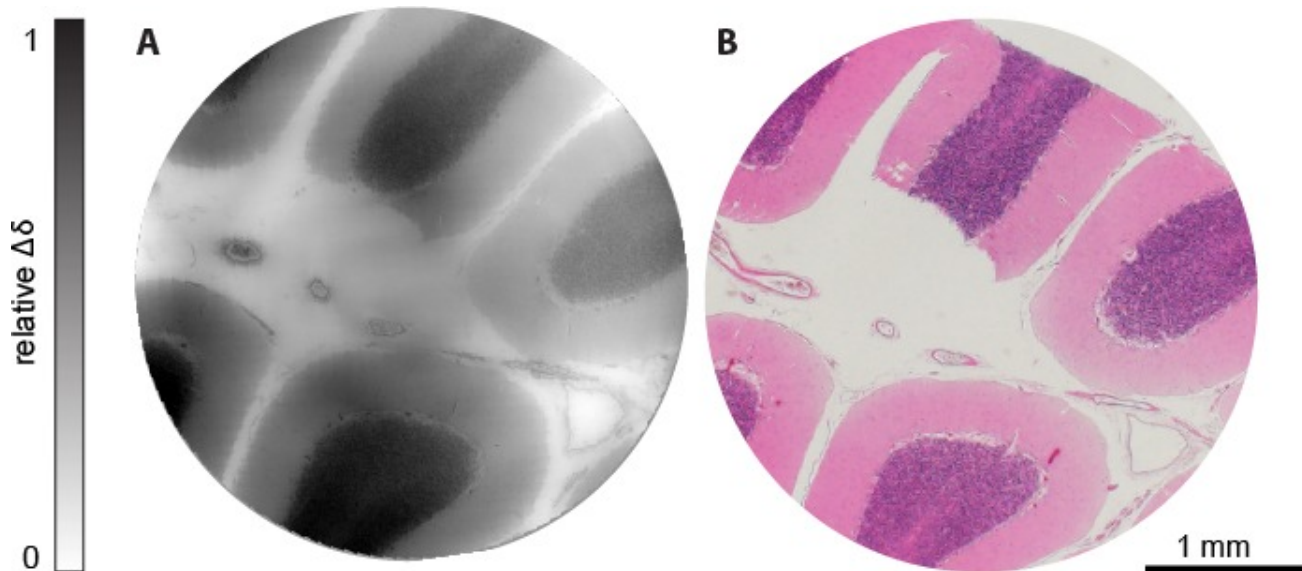
Figure 2. Automatically identified tomography slice (A) in comparison to histological section (B). The 2D-3D registration yields a match for the brain layers, but not for all of the vessels. Although the data set exhibits minor gradients, the intensities of the layers are comparable to one of the histological sections. The Purkinje cells are situated between the two brain layers *Stratum moleculare* and *Stratum granulosum*.

To validate the findings of the brain microstructures, the histological sections of the larger specimen were compared to the tomograms. After the automatic registration, background correction and segmentation of Purkinje cells, the tomographic slide was colored to resemble the histologcial staining. The coloring involved the two colormaps, one for the Purkinje cells and one for the background. The colormaps were fitted to match the typical colors of the cells. Figure 3 shows the clear correspondence of individual neurons including Purkinje cells with a diameter of about 30 μm as well as granule and stellate cells. Even subcelluar details such as dendritic tree and nucleolus are visible. A microvessel can be recognized in the top middle of the region of interest. The result is remarkable and envisions the usage of the three-dimensional data for the analysis of brain diseases in three dimensions.

3.2 Cell quantification

Figure 4 shows the segmentation of the Purkinje cells in a volume of interest. The cell locations form the characteristic shape of the Purkinje cell layer. The identified Purkinje cell layer is situated between two brain layers as expected. The cell volume detected varies over the volume of interest. The variations are slightly influenced by the gradient within the volume of interest, which explains why there are slightly smaller cell volumes in darker regions. As a result larger volumes are more frequently found in the middle of the segmented layer. With an evaluation error of 5% the volume density was found to be 177±6 cells per mm^3 within the volume of interest, which is in agreement with an estimation illustrated in Figure 5.[24]

In the past, high-resolution X-ray tomography was already used to visualize individual ganglion cells in the inner ear[25] and Purkinje cells in the cerebellum[7] without their quantification. Cell density quantification was performed successfully on synchrotron micro-computed tomograms in cow cartilage[26] and mouse brain cortex.[27] These approaches were based on open source software tools and applied to detect spherical cells within tomogram volumes of 1 mm^3 or less.
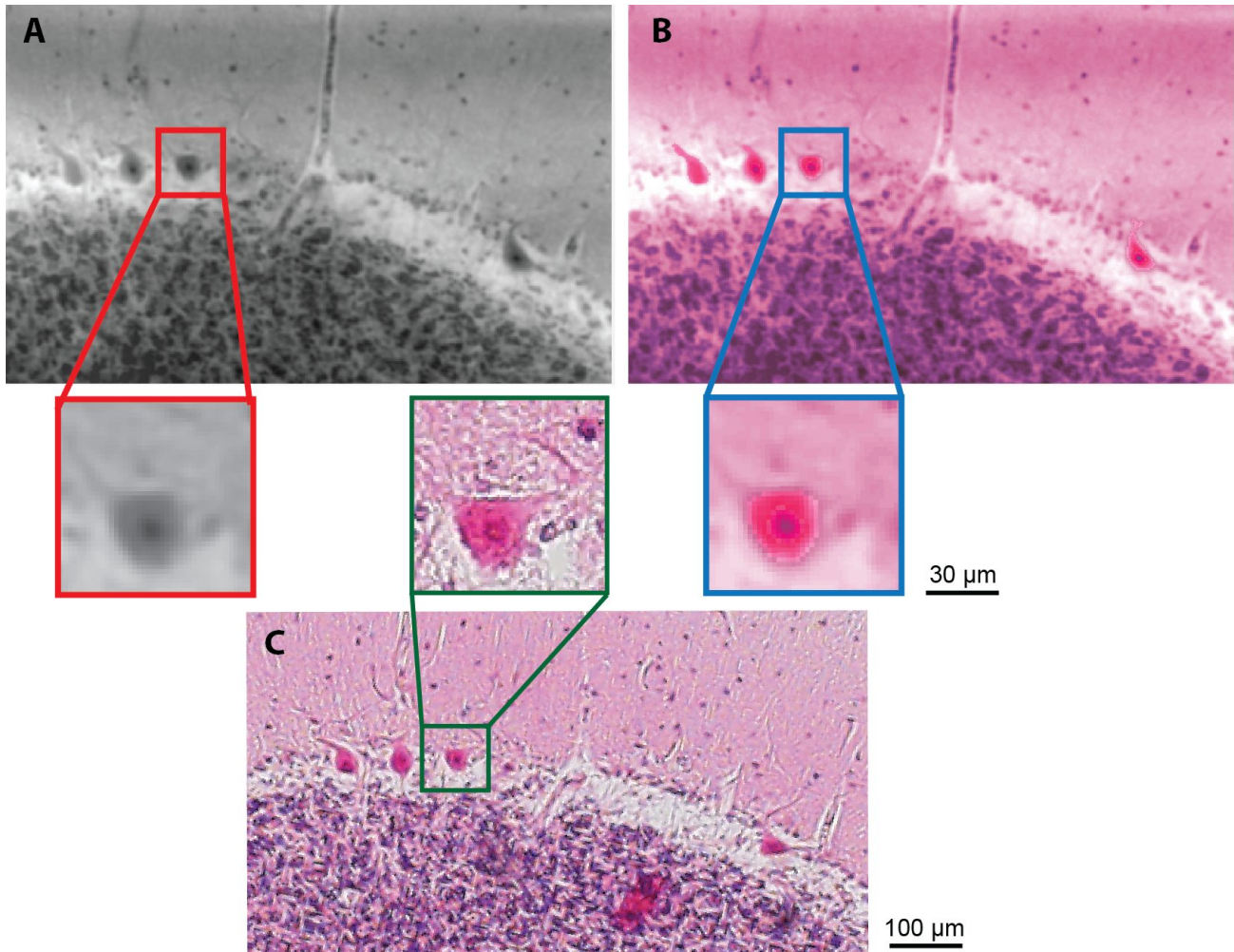
Figure 3. Region of interest in the tomogram (A,B) in comparison to histological section (C) on the cellular level. The slice was registered automatically and is colored to resemble the histological slide. Two colormaps were used, one for the background (white to purple) and one for the Purkinje cells segmented by Frangi-filtering (pink to black). The zoom ins show details of an individual Purkinje cell where the nucleolus is very prominent in dark pink.

To achieve our cell segmentation task we had to develop a dedicated algorithm pipeline different from the standard approaches. Existing automated neuron segmentation approaches are roughly categorized into global and local methods.[28, 29] Global methods rely on an initial separation between the labeled cells that constitute the foreground and the non-labeled structures that constitute the background, followed by a refinement process that differs depending on the specific algorithm implementation. The first step of every global method thus requires the evaluation of information encoded in all image pixels, hence global methods are all computationally expensive. Their alternative, i.e. local methods reduce the computational load by starting the investigation for structures of interest in the vicinity of manually or automatically chosen seeding points. Afterwards, a minimal energy method is employed (e.g. snake or watershed segmentation) to segment the entire neuronal path, with several implementations having been proposed.[30–32] In all cases, the aforementioned approaches, both global and local are designed with microscopy images in mind, where the use of labeling results in a significantly higher signal-to-noise ratio (SNR) than a standard tomography image, due to the fundamental difference between these two modalities. On the other hand, tomography results in images with comparatively lower SNR and a higher structure density.
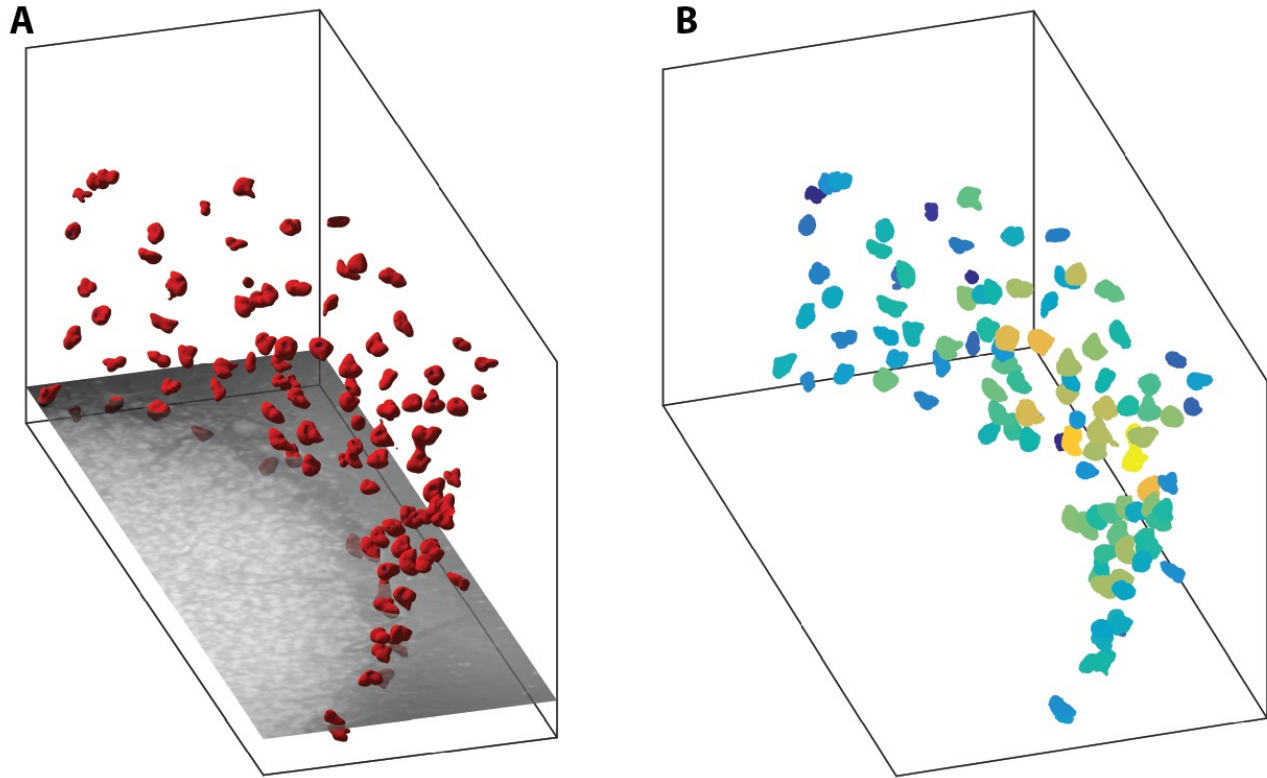
Figure 4. Purkinje cells forming their layer (A) and colored according to cell sizes (B). The segmentation was performed in a volume of interest of size 0.4 mm $\times$ 1.0 mm $\times$ 0.5 mm. The cell volume range covers from 3,000 to 10,000 µm^3. Typically the length of the Purkinje cell is approximately double than its height.
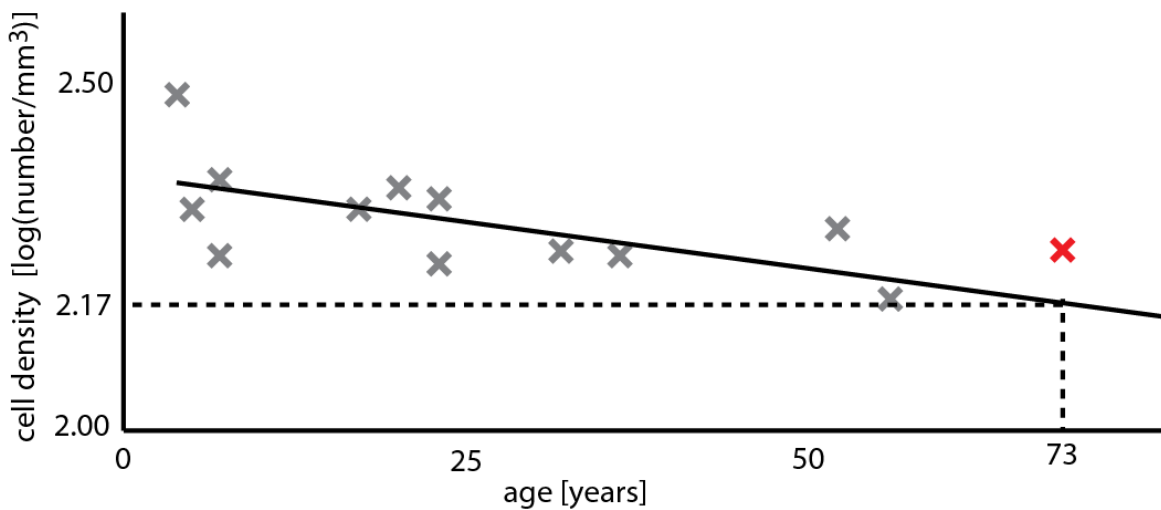

Figure 5. Volume density of Purkinje cells versus age. The extrapolation of the density yields an estimation of 147 cells per mm^3 for a human cerebellum in the age of 73 years, which is close to the determined density of 177 cells per mm^3 (red cross). The data was taken from a medical study related to autism of Skefos *et al.*.[24]

In such cases, the segmentation problem could benefit from the accumulated knowledge on automatic MRI image segmentation for neuronal tractography, where the initial MRI images share similar characteristics to tomography data. Weighting all these factors, we have opted to implement a custom approach, instead of relying

on one of the already published algorithms or open-source software. In detail, we have decided to exploit the complementarity between global and local segmentation methods, which has already been proven to yield superior results, as seen in the case of the APP (All-Path Pruning) algorithms and its derivatives.[33–35] To achieve that, we applied the Frangi filter on the entire initial image in order to select the seeding points for a region-growing step to follow, a strategy that is similar to the one employed by the Tree2Tree algorithm.[36]

3.3 Brain layer segmentation

Figure 6 shows the segmentation result of the Purkinje cells together with the estimation of *Stratum moleculare* (rosa) and *Stratum granulosum* (purple) in a two-dimensional slice. The local gradients were circumvented by the use of edge detection. The edge detection algorithm provides a data set that appears to be gradient-free. Since the determination of the edge density required data binning the accuracy of the brain layer segmentation is limited. But the image yields a realistic estimation of the brain layer areas and their relation to the Purkinje cells.
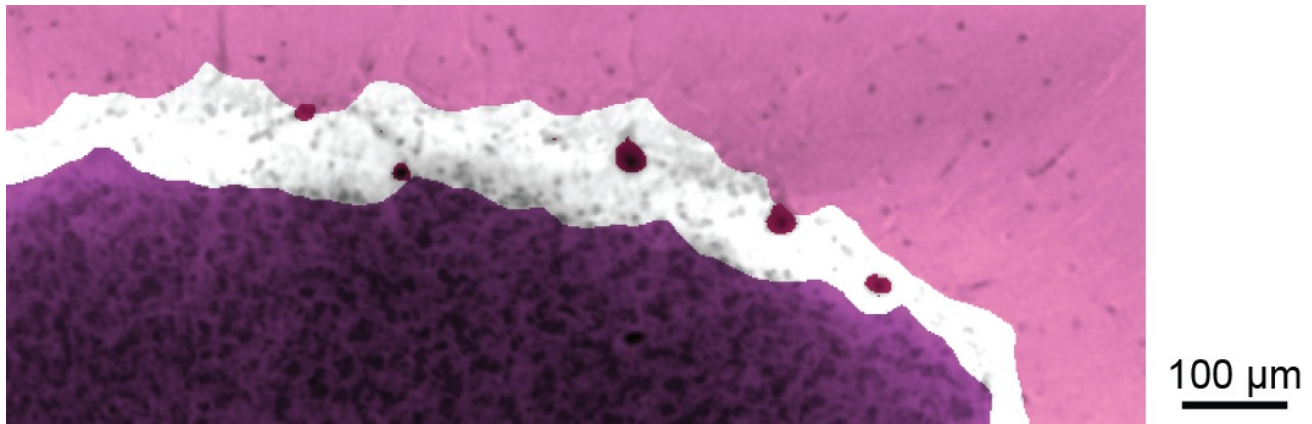

Figure 6. Segmentation of Purkinje cells (dark red), *Stratum moleculare* (rosa) and *Stratum granulosum* (purple) in a tomographic slice. The curved interface forms estimations of the brain layers.

The three-dimensional result of the segmentation (Figure 7) reveals the spreading of the Purkinje cells (pink) along the brain layer. The cell layer remains between the *Stratum granulosum* and *Stratum moleculare*, while a small set of cells is integrated into the *Stratum granulosum*. The volume texture of the brain layers corresponds to the intensities in the tomographic data set. This view confirms as well that the characteristic shape of the Purkinje cells is elliptical.
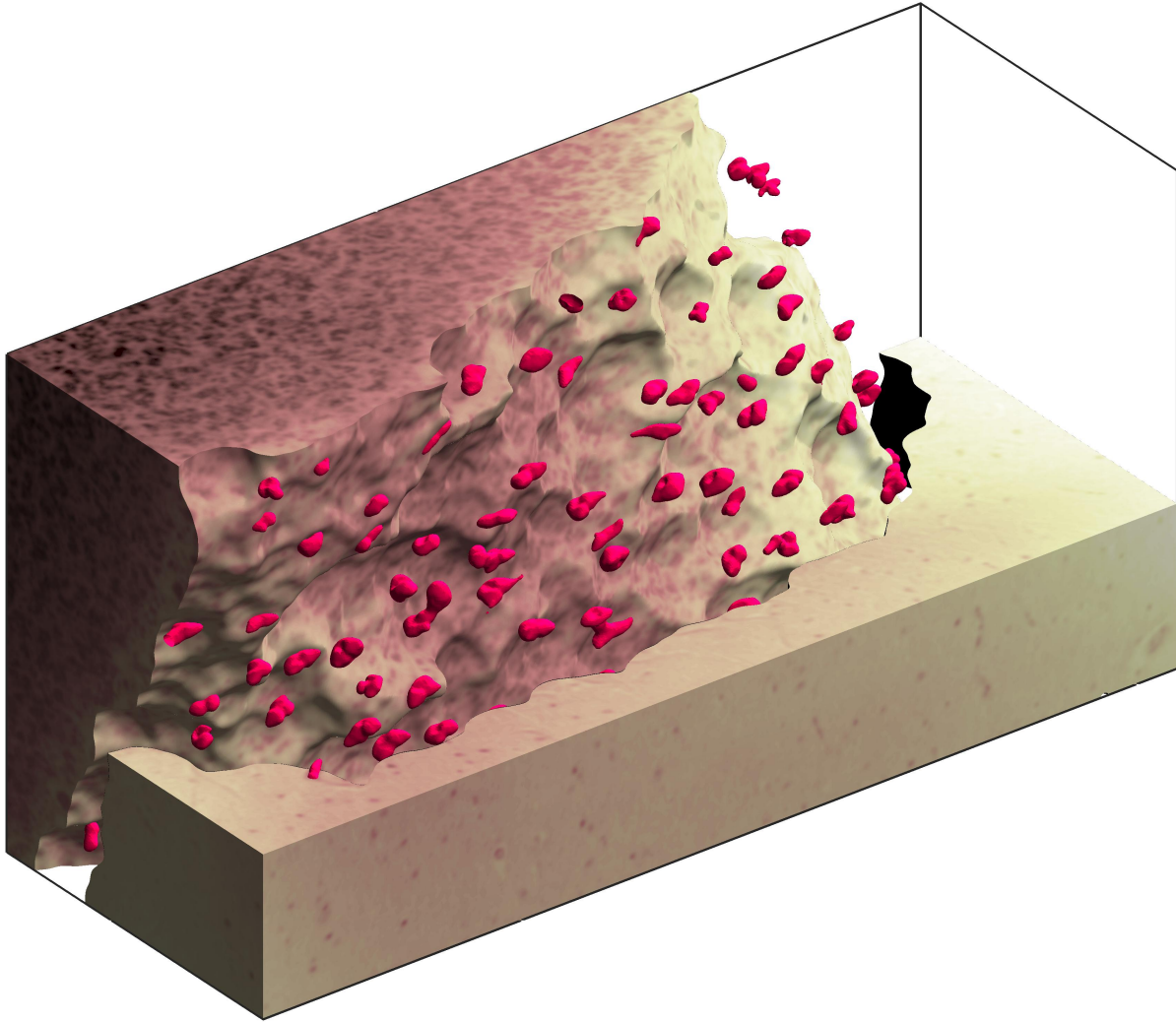
Figure 7. Purkinje cell layer with *Stratum granulosum* and *Stratum moleculare* segmented in 3D over a volume of 0.4 mm × 1.0 mmm × 0.5 mm. The red elliptical shapes correspond to the 102 identifed Purkinje cells. The cells form the characteristic layer, where individual Purkinje cells are integrated into the *Stratum granulosum*.

3.4 Subcellular details of Purkinje cells

The scans with effective pixel size of 0.45 µm reveal the three-dimensional structure of components from Purkinje cells. Figure 9 shows that the results resemble microscopic images of stained histological sections. It has been shown that the modified Weil staining of the histological slice was optimized to visualize the nucleolus for manual Purkinje cell counting by Andersen *et al.*[37] The microscopic image provides a high lateral resolution between 0.2 and 1 µ, but a blurred view on the axial direction due to the slice of 40 µm which is about 10 times thicker than the tomographic slice. Thanks to the isotropic resolution of phase-contrast data set the dendritic tree is significantly better recognizable in the shown slice. Moreover, the microscopic image shows significantly more stellate and granule cells due to the larger thickness of the imaged slice.
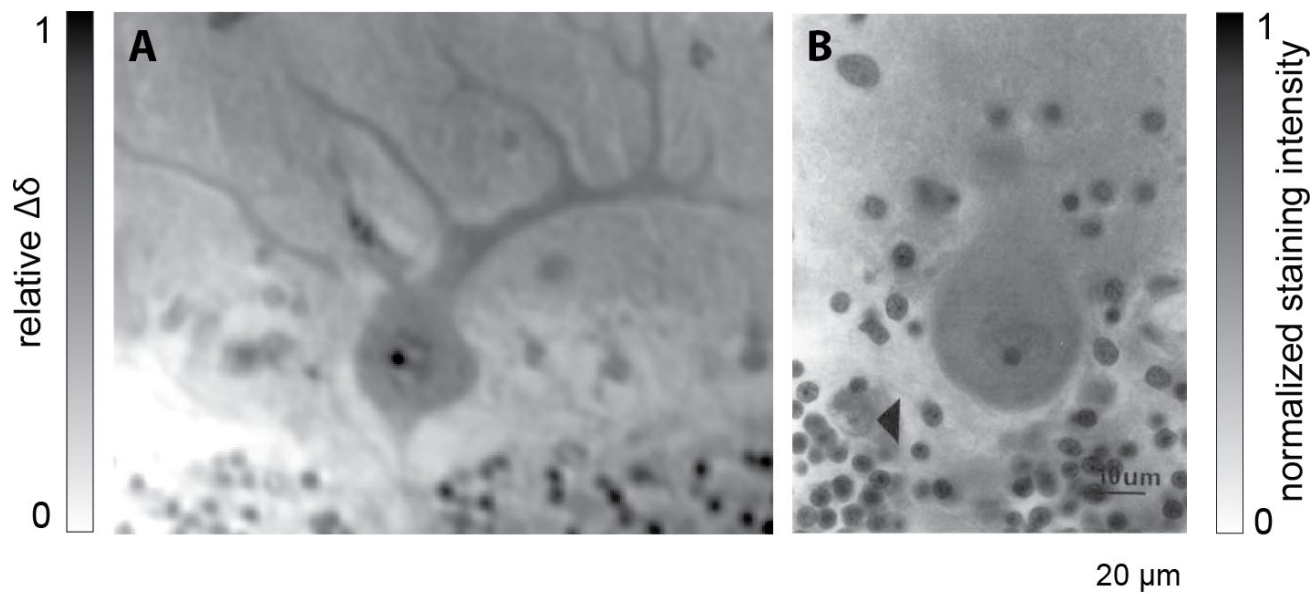
Figure 8. Purkinje cell including main dendritic tree represented in a tomogram slice and a histological slide. clear correspondence with respect to the cell morphology, in particular the nucleolus and surrounding the nucleus. The nucleolus is characterized by a high contrast in both cases. The Weil-stained histological slide is extracted from the literature[37] [copyright acquire with license number: 3946990838994].
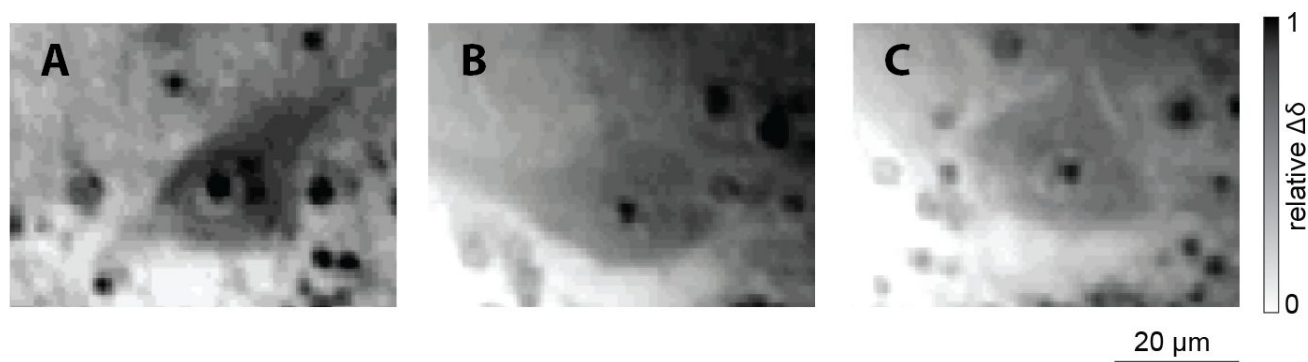

Figure 9. Selected Purkinje cells from the phase-contrast data set. The nuclei are clearly visible around the prominent nucleoli which are well recognizable as dark spots in the center of the cell.

Figure 9 shows the variety of the appearance of the Purkinje cells that have an elliptic shape in general. The nuclei always surround the nucleoli featuring a prominent phase shift which simplifies the identification of cells. Similar situations in histology have already been exploited for the quantitative study of the cerebellum.[37]

4. SUMMARY AND OUTLOOK

In this study we present a complete pipeline from specimen preparation with paraffin embedding, data acquisition using single-distance propagation based phase retrieval to cell quantification. The results were validated using a comparison with histological sectioning. The cells were automatically identified based on specifically a designed filter in three dimensions, which envisions the large scale analysis of tissue on the cellular basis. Moreover, brain layers were segmented in three dimensions to reveal locations of the Purkinje cell layer with respect to the brain layer interface. We expect that the methodology can also be applied to other soft tissues and advance the computational analysis of cells and their accuracy.

5. ACKNOWLEDGEMENTS

REFERENCES

[1] Miura, K., "On the function of the cerebellum," *Science* **58**(1506), 361–2 (1923).

[2] Desmond, J. E. and Fiez, J. A., "Neuroimaging studies of the cerebellum: Language, learning and memory," *Trends Cogn. Sci.* **2**(9), 355–62 (1998).

[3] Benard, M., Lebon, A., Komuro, H., Vaudry, D., and Galas, L., "Ex vivo imaging of postnatal cerebellar granule cell migration using confocal macroscopy," *J. Vis. Exp.* (99) (2015).

[4] Silvestri, L., Bria, A., Costantini, I., Sacconi, L., Peng, H., Iannello, G., and Pavone, F. S., "Micron-scale resolution optical tomography of entire mouse brains with confocal light sheet microscopy," *J. Vis. Exp.* (80) (2013).

[5] Wang, H., Zhu, J., and Akkin, T., "Serial optical coherence scanner for large-scale brain imaging at microscopic resolution," *Neuroimage* **84**, 1007–17 (2014).

[6] Chung, K., Wallace, J., Kim, S. Y., Kalyanasundaram, S., Andalman, A. S., Davidson, T. J., Mirzabekov, J. J., Zalocusky, K. A., Mattis, J., Denisin, A. K., Pak, S., Bernstein, H., Ramakrishnan, C., Grosenick, L., Gradinaru, V., and Deisseroth, K., "Structural and molecular interrogation of intact biological systems," *Nature* **497**(7449), 332–7 (2013).

[7] Schulz, G., Weitkamp, T., Zanette, I., Pfeiffer, F., Beckmann, F., David, C., Rutishauser, S., Reznikova, E., and Müller, B., "High-resolution tomographic imaging of a human cerebellum: Comparison of absorption and grating-based phase contrast," *J. R. Soc. Interface* **7**(53), 1665–76 (2010).

[8] Pfeiffer, F., David, C., Bunk, O., Poitry-Yamate, C., Grtter, R., Müller, B., and Weitkamp, T., "High-sensitivity phase-contrast tomography of rat brain in phosphate buffered saline," *J. Phys: Conf. Ser.* **186**, 012046 (2009).

[9] Khimchenko, A., Deyhle, H., Schulz, G., Schweighauser, G., Hench, J., Chicherova, N., Bikis, C., Hieber, S. E., and Müller, B., "Extending two-dimensional histology into the third dimension through conventional micro computed tomography," *Neuroimage* **139**, 26–36 (2016).

[10] Hieber, S. E., Bikis, C., Khimchenko, A., Schweighauser, G., Hench, J., Chicherova, N., Schulz, G., and Müller, B., "Tomographic brain imaging with nucleolar detail and automatic cell counting," *Sci. Rep.* **6**, 32156 (2016).

[11] Weitkamp, T., Tafforeau, P., Boller, E., Cloetens, P., Valade, J., Bernard, P., Peyrin, F., Ludwig, W., Helfen, L., and Baruchel, J., "Status and evolution of the ESRF beamline ID19," in [*AIP Conference Proceedings*], **1221**, 33–38 (2010).

[12] Rau, C., Wagner, U., Pesic, Z., and Fanis, A. D., "Coherent imaging at the Diamond beamline I13," *Phys. Stat. Sol. A* **208**(11), 2522–2525 (2011).

[13] Lang, S., Zanette, I., Dominietto, M., Langer, M., Rack, A., Schulz, G., Duc, G. L., David, C., Mohr, J., Pfeiffer, F., Müller, B., and Weitkamp, T., "Experimental comparison of grating- and propagation-based hard X-ray phase tomography of soft tissue," *J. Appl. Phys.* **116**, 154903 (2014).

[14] Zanette, I., Lang, S., Rack, A., Dominietto, M., Langer, M., Pfeiffer, F., Weitkamp, T., and Müller, B., "Holotomography versus X-ray grating interferometry: A comparative study," *Applied Physics Letters* **103**, 244105 (2013).

[15] Weitkamp, T., Haas, D., Wegrzynek, D., and Rack, A., "ANKAphase: Software for single-distance phase retrieval from inline X-ray phase-contrast radiographs," *J. Synchrotron Rad.* **18**(4), 617 (2011).

[16] Münch, B., Trtik, P., Marone, F., and Stampanoni, M., "Stripe and ring artifact removal with combined wavelet-fourier filtering," *EMPA Activities* **17**(2009-2010), 34–35 (2009).

[17] Stalder, A. K., Ilgenstein, B., Chicherova, N., Deyhle, H., Beckmann, F., Müller, B., and Hieber, S. E., "Combined use of micro computed tomography and histology to evaluate the regenerative capacity of bone grafting materials," *Int. J. Mater. Res.* **105**(7), 679–691 (2014).

[18] Chicherova, N., Fundana, K., Müller, B., and Cattin, P. C., "Histology to CT data matching using landmarks and a density biased RANSAC," *Med. Image Comput. Comput.- Assist. Interv.* , 243–250 (2014).

[19] Bay, H., Ess, A., Tuytelaars, T., and Van Gool, L., "Speeded-up robust features (SURF)," *Comp. Vis. Image Underst.* **110**(3), 346–359 (2008).

[20] Shechtman, E. and Irani, M., "Matching local self-similarities across images and videos," *Comp. Vis. Patt. Recog.* , 1–8 (2007).

[21] Basu, M., "Gaussian-based edge-detection methods-a survey," *IEEE Trans. Syst., Man, and Cyb.* **32**(3), 252–260 (2002).

[22] Thurner, P., Beckmann, F., and Müller, B., "An optimization procedure for spatial and density resolution in hard X-ray micro-computed tomography," *Nucl. Instr. Meth. Phys. Res. Sec. B* **225**(4), 599–603 (2004).

[23] Otsu, N., "A threshold selection method from gray-level histograms," *IEEE Trans. Syst., Man and Cyb.* **9**(1), 62–66 (1979).

[24] Skefos, J., Cummings, C., Enzer, K., Holiday, J., Weed, K., Levy, E., Yuce, T., Kemper, T., and Bauman, M., "Regional alterations in purkinje cell density in patients with autism," *PLoS One* **9**(2), e81255 (2014).

[25] Lareida, A., Beckmann, F., Schrott-Fischer, A., Glueckert, R., Freysinger, W., and Müller, B., "High-resolution X-ray tomography of the human inner ear: synchrotron radiation-based study of nerve fibre bundles, membranes and ganglion cells," *J. Microscopy* **234**(1), 95–102 (2009).

[26] Zehbe, R., Haibel, A., Riesemeier, H., Gross, U., Kirkpatrick, C. J., Schubert, H., and Brochhausen, C., "Going beyond histology. synchrotron micro-computed tomography as a methodology for biological tissue characterization: from tissue morphology to individual cells," *J. R. Soc. Interface* **7**(42), 49–59 (2010).

[27] Dyer, E. L., Roncal, W. G., Fernandes, H. L., Grsoy, D., Xiao, X., Vogelstein, J. T., Jacobsen, C., Kording, K. P., and Kasthuri, N., "Quantifying mesoscale neuroanatomy using x-ray microtomography," *arXiv preprint* , arXiv:1604.03629 (2016).

[28] Meijering, E., "Neuron tracing in perspective," *Cytometry A* **77**(7), 693–704 (2010).

[29] Donohue, D. E. and Ascoli, G. A., "Automated reconstruction of neuronal morphology: An overview," *Brain Res. Rev.* **67**(1-2), 94–102 (2011).

[30] Al-Kofahi, Y., Lassoued, W., Lee, W., and Roysam, B., "Improved automatic detection and segmentation of cell nuclei in histopathology images," *IEEE Trans. Biomed. Eng.* **57**(4), 841–52 (2010).

[31] Al-Kofahi, Y., Dowell-Mesfin, N., Pace, C., Shain, W., Turner, J. N., and Roysam, B., "Improved detection of branching points in algorithms for automated neuron tracing from 3d confocal images," *Cytometry A* **73**(1), 36–43 (2008).

[32] Al-Kofahi, K. A., Lasek, S., Szarowski, D. H., Pace, C. J., Nagy, G., Turner, J. N., and Roysam, B., "Rapid automated three-dimensional tracing of neurons from confocal image stacks," *IEEE Trans. Inf. Technol. Biomed.* **6**(2), 171–87 (2002).

[33] Peng, H., Long, F., and Myers, G., "Automatic 3d neuron tracing using all-path pruning," *Bioinformatics* **27**(13), i239–47 (2011).

[34] Xiao, H. and Peng, H., "App2: automatic tracing of 3d neuron morphology based on hierarchical pruning of a gray-weighted image distance-tree," *Bioinformatics* **29**(11), 1448–54 (2013).

[35] Liu, S., Zhang, D., Liu, S., Feng, D., Peng, H., and Cai, W., "Rivulet: 3d neuron morphology tracing with iterative back-tracking," *Neuroinformatics* (2016).

[36] Basu, S., Condron, B., Aksel, A., and Acton, S., "Segmentation and tracing of single neurons from 3D confocal microscope images," *IEEE J. Biomed. Health Inform.* **17**(2), 319–35 (2013).

[37] Andersen, B. B., Korbo, L., and Pakkenberg, B., "A quantitative study of the human cerebellum with unbiased stereological techniques," *J. Comp. Neurol.* **326**(4), 549–560 (1992).